Icarus 272 (2016) 277–289

Contents lists available at ScienceDirect

Icarus

journal homepage: www.elsevier.com/locate/icarus

Dione and Rhea seasonal exospheres revealed by Cassini CAPS and INMS

B.D. Teolis*, J.H. Waite

Space Science Division, Southwest Research Institute, San Antonio, TX 78230, USA

ARTICLE INFO

Article history:
Received 8 July 2015
Revised 8 January 2016
Accepted 22 February 2016
Available online 2 March 2016

Keywords:
Atmospheres
Dynamics atmospheres
Evolution atmospheres
Structure satellites
Atmospheres Saturn
Satellites

ABSTRACT

A Dione O_2 and CO_2 exosphere of similar composition and density to Rhea's is confirmed by Cassini spacecraft Ion Neutral Mass Spectrometer (INMS) flyby data. INMS results from three Dione and two Rhea flybys show exospheric spatial and temporal variability indicative of seasonal exospheres, modulated by winter polar gas adsorption and desorption at the equinoxes. Cassini Plasma Spectrometer (CAPS) pickup ion fluxes also show exospheric structure and evolution at Rhea consistent with INMS, after taking into consideration the anticipated charge exchange, electron impact, and photo-ionization rates. Data-model comparisons show the exospheric evolution to be consistent with polar frost diffusion into the surface regolith, which limits surface exposure and loss of the winter frost cap by sputtering. Implied O_2 source rates of $\sim 45(7) \times 10^{21}$ s^{-1} at Dione(Rhea) are ~50(300) times less than expected from known O_2 radiolysis yields from ion-irradiated pure water ice measured in the laboratory, ruling out secondary sputtering as a major exospheric contributor, and implying a nanometer scale surface refractory lag layer consisting of concentrated carbonaceous impurities. We estimate ~30:1(2:1) relative O_2:CO_2 source rates at Dione(Rhea), consistent with a stoichiometric bulk composition below the lag layer of 0.01(0.13) C atoms per H_2O molecule, deriving from endogenic constituents, implanted micrometeoritic organics, and (in particular at Dione) exogenous H_2O delivery by E-ring grains. Impact deposition, gardening and vaporization may thereby control the global O_2 source rates by fresh H_2O ice exposure to surface radiolysis and trapped oxidant ejection.

1. Introduction

Radiolytic oxygen and carbon dioxide exospheres have been observed remotely at several Solar System icy satellites, with O_2 detected at the Galilean satellites Ganymede and Europa (Hall et al., 1998; McGrath et al., 2013; Saur et al., 2011), and O_2 and CO_2 identified at Callisto (Carlson, 1999; Cunningham et al., 2015). Extrapolating to the Saturn system, Sittler et al. (2004) and Saur and Strobel (2005) made the first exospheric estimates at the large Saturnian icy satellites, and CAPS magnetospheric (Martens et al., 2008) and pickup ion data (Jones et al., 2009) gave indications of a possible Rhea exospheric source shortly after Cassini's arrival. In 2010 Cassini INMS (Waite et al., 2004) performed the first direct sampling of a radiolytic icy satellite exosphere during the close (100 km) north polar R2 Rhea flyby, and verified the existence of an O_2:CO_2 exosphere (Teolis et al., 2010a). The molecular oxygen may be ejected following radiolysis through surface ice radiation chemistry by impinging solar UV photons and magnetospheric particles (Johnson et al., 2013; Teolis et al., 2009), while CO_2 may be synthesized by radiolysis of water-derived O atoms with endogenic and/or implanted organics (Clark et al., 2008; Cruikshank et al., 2010). The R2 flyby trajectory across Rhea's polar terminator enabled both the day and night hemispheres to be sampled, revealing that CO_2 was concentrated over the dayside; a finding consistent with a 'sticky' exosphere adsorbed onto cold night side and polar terrains. Recently Simon et al. (2011) have attributed Dione magnetic field signatures to an exosphere, and Tokar et al. (2012) have identified O_2^+ pickup ions (PUI) from Dione CAPS spectra, thereby confirming an exospheric O_2 source.

In this paper we analyze Cassini's 72 km Rhea south polar encounter (R3) on 11 Jan 2011, and the 99 km equatorial Dione flyby (D3) on 12 Dec 2011 (Table 1), during which INMS again detected O_2 and CO_2 exospheres of similar density and composition at both bodies (Teolis and Waite, 2012). The INMS data show that Dione's exosphere, like Rhea's, is also concentrated over the dayside hemisphere (Fig. 1). The INMS Dione neutral densities ($\sim 1(3) \times 10^{10}$ $O_2(CO_2)/m^3$ at the 99 km flyby altitude) are below the Cassini Magnetometer (MAG)

* Corresponding author. Tel.: +0012105225975.
E-mail address: ben.teolis@swri.org, bteolis@swri.edu (B.D. Teolis).

http://dx.doi.org/10.1016/j.icarus.2016.02.031

Table 1
Dione and Rhea flyby observations.

Flyby	Body	Date	UTC	Speed	Alt	Detection	Species	References	Description
D1	Dione	11-Oct-05	17:52:00	9.12 km/s	500 km	MAG	–	Simon et al. (2011)	Upstream southern flux tube, Saturn inbound.
R1	Rhea	26-Nov-05	22:37:38	7.28	500	CAPS	CO_2^+	Teolis et al. (2010), This work	Equatorial wake, toward night side, Saturn inbound.
R1.5	Rhea	30-Aug-07	01:18:55	6.76	5725	CAPS	$CO_2^{+,\ O-}$	This work	Northern wake, toward night side, Saturn outbound.
R2	Rhea	2-Mar-10	17:40:36	8.58	100	INMS	O_2, CO_2	Teolis et al. (2010), This work	Low altitude, north polar, toward day side, Saturn inbound.
D2	Dione	7-Apr-10	05:16:11	8.34	500	CAPS	O_2^+	Tokar et al. (2012)	Equatorial wake, toward day side, Saturn inbound.
R3	Rhea	11-Jan-11	04:53:25	8.05	72	INMS	O_2	This Work	Low altitude, south polar, toward day side, Saturn outbound.
D3	Dione	12-Dec-11	09:39:23	8.73	99	INMS	O_2, CO_2	This Work	Low altitude, equatorial wake, toward day side, Saturn outbound. CAPS offline.
R4	Rhea	9-Mar-13	18:17:26	9.29	996	–	none	This work	South-to-north, over anti-Saturn night side. CAPS offline. Altitude too high, and pointing poor, for INMS: Non-detection
D4	Dione	16-Jun-15	20:11:52	7.32	516	INMS	O_2	This work	North polar, toward night side, Saturn outbound. CAPS offline.
D5	Dione	17-Aug-15	18:33:25	6.45	476	–	none	This work	North polar, toward night side, Saturn inbound. CAPS offline.

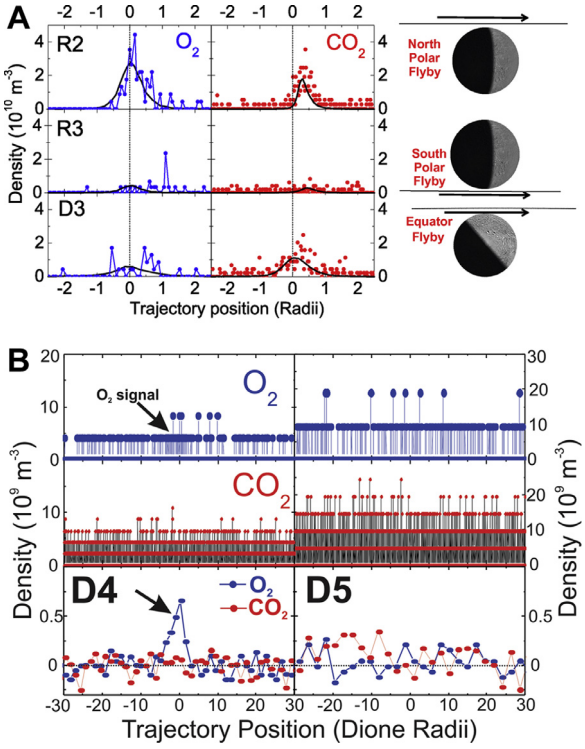

Fig. 1. (A) The Dione and Rhea O_2 and CO_2 exospheric densities measured by Cassini INMS versus distance (in planetary radii) from closest approach (dashed line) along the night-to-day R2, R3 and D3 trajectories (shown on right). The data are un-binned, such that single counts are visible. INMS measured the neutral gas ram flux encountered by the spacecraft with 2π steradians FOV on all flybys. We have used the newly updated INMS calibration model (Teolis et al., 2015), correcting for spacecraft speed and pointing, to estimate the densities. Time increases left to right in the plots, with Cassini moving from the night to the day side hemisphere on all flybys. As shown, the exospheric profiles are concentrated (especially for CO_2) over the dayside when equivalent inbound–outbound altitudes are compared. Lines: exosphere model results. (B) Exospheric data (Top, Center: raw counts converted to density, Bottom: binned/background subtracted) from the recent Dione northern high (516 km) altitude (day-to-night) D4 and D5 flybys, showing the detection of O_2 but not CO_2 at D4, and the non-detection of either species at D5. Time increases left to right with Cassini moving from the day to the night side hemisphere on both flybys.

based estimate (8×10^{11} molecules/m^3 (Simon et al., 2011)), but within the range of O_2 surface density ($0.6–5 \times 10^{10}$ O_2/m^3 (Tokar et al., 2012)) implied by CAPS. INMS has also detected O_2 during the recent Dione north polar flyby (D4) on 16 Jun 2015, albeit at lower ($\sim 0.05 \times 10^{10}$ O_2/m^3) density (Fig. 1b) due to the high (516 km) flyby altitude. The existence of exospheres with comparable densities and compositions at Dione and Rhea suggests that similar physical processes drive their exospheres, since these bodies have sufficient mass (1.1 and 2.3×10^{21} kg, respectively) to retain the neutral gas, and both orbit in the inner magnetosphere at 6.3 and 8.8 R_S, where their surfaces are subject to similar magnetospheric particle fluxes ($\sim$9(15), 36(10), 48(73) $\times 10^{26}$ eV/s from water group ions, protons and electrons at Dione(Rhea), as estimated from Table 3 references). The direct capture and analysis of the neutral gas by INMS, performed at different times and locations around two icy bodies of similar size, mass and composition, have provided a first of its kind opportunity to sample in situ at an icy satellite the composition, spatial distribution and temporal evolution of the radiolytic exosphere.

2. Results

The INMS data (Fig. 1) show major variations in gas density and composition (1) spatially along Cassini's trajectory (2) and temporally between flybys. The CO_2 and O_2 densities are asymmetrical about Cassini's closest approach points at both Dione and Rhea, with higher densities consistently observed over the daysides of both satellites on all flybys when equivalent inbound–outbound altitudes are compared. The day–night difference is consistent with surface thermal adsorption, which sequesters more molecules onto the colder night side and polar regions. CO_2 is less volatile than O_2 (with 236 and 90 K boiling points, respectively), which may account for the more pronounced day–night asymmetry in the CO_2 data compared to O_2.

However the south polar R3 flyby presents a puzzle, as much less gas was detected than the earlier 100 km R2 north polar flyby, despite the similar polar geometry of both encounters and the lower 72 km R3 flyby altitude. As shown in Fig. 1 INMS detected $\sim 2 \times 10^{10}$ CO_2 per m^3 over the Rhea north pole at R2, but then did not detect CO_2 at R3 above an upper limit of 0.7×10^{10} m^{-3}. Thermal adsorption, as implied by the CO_2 exospheric day/night asymmetry, may be responsible for the lack of CO_2 over Rhea's southern latitudes, which are presently cooling as the Saturn system approaches southern winter. More difficult to explain at Rhea is the lack of O_2 in the south: $\sim$0.5, versus $\sim 5 \times 10^{10}$ m^{-3} in the north (Fig. 1), since O_2 is more volatile than CO_2.

To shed light on these questions we applied a Monte Carlo collisionless exosphere code to model the Dione and Rhea exospheres, including the surface adsorption effects as implied by the

Table 2
Summary of techniques incorporated into our exospheric modeling, and examples of previous applications to other Solar System bodies. References: (1) (Cassidy, 2008; Cassidy et al., 2007; Plainaki et al., 2010; Plainaki et al., 2012; Shematovich et al., 2005; Smyth and Marconi, 2006), (2) (Marconi, 2007; Plainaki et al., 2015), (3) (Vorburger et al., 2015), (4) (Teolis et al., 2010a), (5) (Burger et al., 2010; Crider and Vondrak, 2000; Killen et al., 2012; Shim, 2001), (6) (Paige et al., 2010; Siegler et al., 2012), (7) (Paige et al., 2012).

Technique	How used	References
Monte Carlo exosphere	Position and temperature-dependent surface source distribution, particles "hop" around Moon on ballistic trajectories, loss processes included: Jeans escape, ionization, dissociation, charge exchange. Gives altitude profile, spatial distribution of surface sputter products.	At icy satellites: Europa (1) Ganymede (2) Callisto (3) Rhea (4)
"Sticky" exosphere models.	Monte Carlo model same as above, except molecules allowed to stick transiently on surface for temperature-dependent time. Requires surface temperature model versus time, accounting for planet rotation.	Moon (5)
Thermal and gas adsorption and diffusion	Solar illumination and shadowing, subsurface heat diffusion considered to produce temperature map versus position and depth. Thermal results used to predict gas diffusion, trapping versus position and depth.	Moon (6) Mercury (7)

Table 3
Average exospheric O_2 loss rates (units 10^{-8}/s/molecule), estimated as explained in the Appendix. Solar rates (quiet / active Sun outside/inside parentheses) directly from Huebner et al. (1992) scaled to 9.6 A.U: we applied quiet (active) rates at R1,R1.5,R2,R3,D3 (D4,D5) consistent with solar activity on those dates. Ion and electron rates estimated by convolving published energy-dependent cross sections and Cassini CAPS/MIMI plasma flux-versus-energy spectra, see Appendix. For total loss rate estimates (Table 4) we treat O^+ as a proxy for magnetospheric "water group" ions consisting of O^+, OH^+, H_2O^+, and H_3O^+ (Wilson et al., 2010). References: (1) (Dialynas et al., 2009; Thomsen et al., 2010; Wilson et al., 2008; Wilson et al., 2010), (2) (Schippers et al., 2008), (3) (Huebner et al., 1992), (4) (Itikawa, 2008), (5) (Luna et al., 2005), (6) (Sieglaff et al., 2000), (7) (Cabrera-Trujillo et al., 2004; Williams et al., 1984).

Loss channel	Rhea	Dione	References	
			cross sections	Flux spectra
$O^+ + O_2 \rightarrow O + O_2^+$	0.68	1.5	5, 6	1
$O^+ + O_2 \rightarrow O + O^+ + O$	0.24	0.54	5, 6	1
$O^+ + O_2 \rightarrow O + 2O^+ + e$	0.023	0.041	5, 6	1
$O^+ + O_2 \rightarrow O + O^{++} + O + e$	0.0003	0.00012	5, 6	1
$O^+ + O_2 \rightarrow O^+ + O_2^+ + e$	0.11	0.28	5, 6	1
$O^+ + O_2 \rightarrow O^+ + O^+ + O + e$, $O^+ + O_2 \rightarrow O^+ + 2O^+ + 2e$	0.072	0.058	5, 6	1
$O^+ + O_2 \rightarrow O^+ + O^{++} + O + 2e$	0.0081	0.0064	5, 6	1
$H^+ + O_2 \rightarrow H + O_2^+$	0.59	1.1	5, 7	1
$H^+ + O_2 \rightarrow H + O^+ + O$	0.032	0.062	5, 7	1
$H^+ + O_2 \rightarrow H + 2O^+ + e$	0.0084	0.018	5, 7	1
$H^+ + O_2 \rightarrow H + O^{++} + O + e$	0.0004	0.0012	5, 7	1
$H^+ + O_2 \rightarrow H^+ + O_2^+ + e$	0.018	0.044	5, 7	1
$H^+ + O_2 \rightarrow H^+ + O^+ + O + e$, $H^+ + O_2 \rightarrow H^+ + 2O^+ + 2e$	0.018	0.041	5, 7	1
$H^+ + O_2 \rightarrow H^+ + O^{++} + O + 2e$	0.018	0.041	5, 7	1
$e + O_2 \rightarrow O_2^+ + 2e$	2.2	0.55	4	2
$e + O_2 \rightarrow O^+ + O + 2e$, $e + O_2 \rightarrow 2O^+ + 3e$	0.95	0.19	4	2
$e + O_2 \rightarrow O^{++} + O + 3e$, $e + O_2 \rightarrow 2O^{++} + 5e$	0.011	0.0013	4	2
$e + O_2 \rightarrow O + O + e$	0.89	0.42	4	2
$e + O_2 \rightarrow O + O^-$	0.0022	0.0058	4	2
$v + O_2 \rightarrow O(3P) + O(3P)$	0.081(0.120)	0.081(0.120)	3	
$v + O_2 \rightarrow O(3P) + O(1D)$	2.2(3.5)	2.2(3.5)	3	
$v + O_2 \rightarrow O(1S) + O(1S)$	0.022(0.053)	0.022(0.053)	3	
$v + O_2 \rightarrow O_2^+ + e$	0.26(0.66)	0.26(0.66)	3	
$v + O_2 \rightarrow O + O^+ + e$	0.061(0.192)	0.061(0.192)	3	
Jeans Escape	13	38		
TOTAL	22(24)	46(48)		

INMS flyby data; Table 2 summarizes the modeling techniques and their application at other Solar System bodies. The model tracked (in 150 s time steps) the ballistic trajectories of O_2 and CO_2 molecules ejected with a cosine angular distribution of flux from random surface source locations, with a constant latitude/longitude dependent surface source distribution (predominantly radiolysis/sputtering by ions) according to the model described by Teolis et al. (2010b). The molecules were ejected with a 30/70% mixed sputter/thermalized distribution of speeds as appropriate for volatile sputtering from a surface regolith (Cassidy and Johnson, 2005). We neglected intermolecular collisions since the molecular mean free path is still ~3000 km, even at the maximum Dione and Rhea surface gas densities (~10^{12} molecules/m^3, see below), which is still much greater than the mean flight path (420(320) km for Dione(Rhea) O_2) between molecular surface impacts. We allowed neutral molecules to leave the simulation space ($5 \times 5 \times 5$ body radii) gravitationally, and also removed neutrals stochastically in flight according to the estimated photo and impact ionization and dissociative and charge exchange collision rates (Table 3), which we obtained for O_2 by convolving laboratory cross sections with solar and Cassini magnetospheric particle flux distributions versus energy as described in the Appendix. Published CO_2 cross sections are not as extensive as O_2 (in particular for the ion channels) and, accordingly, we have elected (with the exception of gravitational escape) to assume for now the same total ionization/loss rates (Table 4) for CO_2 as for O_2. The estimated $O_2(CO_2)$ average lifetimes in-flight (not including surface sticking), given by the inverse of the total loss rates (Tables 3–4), are $2.2(3.6) \times 10^6$ s at Dione ($4.5(10.4) \times 10^6$ s at Rhea). Since these times are sufficient for thermal gas moving at hundreds of m/s to diffuse around the moon, the exospheric structure is decorrelated from the spatial distribution of sputtering and of ionization/loss. The model exospheres are also (except near solstice) insensitive to magnetospheric temporal variability for reasons discussed below. Accordingly, the

Table 4
Modeled exospheric sources and sinks. O_2 loss rates summed from Table 3. Row groupings: same units. Rates for quiet/active Sun are outside/inside parentheses.

	Units	Rhea		Dione	
		O_2	CO_2	O_2	CO_2
Avg in-flight abundance[a]	10^{28} molecules	3.3	3.9	9.7	0.57
Time to Escape[b]	Earth years	2.7	700	2.5	160
Jeans escape rate	10^{-8} /s/molecule	13	1.0	38	20
Dissociative channels[c]		4.7(6.1)		3.8(5.2)	
e-Impact ionization		2.2		0.55	
Photo-ionization		0.26(0.66)		0.26(0.66)	
ion-impact ionization		0.13		0.33	
Charge exchange ionization		1.3		2.6	
Total ionization[e]		3.9(4.3)	3.9[d]	3.7(4.1)	3.7[c]
Total loss rate		22(24)	9.6(11.6)	46(48)	28(30)
Expected source rate[f]	10^{21} molecules/s	2200		2100	
Observed source rate[g]		7.2	3.7	45	1.6
Exp sputter yield[h]		2.7		1.4	
Obs sputter yield[h,i]	molecules / ion	0.0088	0.0045	0.029	0.0010
Expected/Observed	none	306		47	

[a] Total number of exospheric molecules, time averaged over a season.
[b] Includes time stuck to surface.
[c] All dissociation and dissociative ionization channels (Table 3).
[d] Taking O_2 rate: Insufficient published cross sections to estimate CO_2 independently to same accuracy as O_2.
[e] Sums e-impact, ion-impact, photo, charge exchange rows, leading only to O_2^+, CO_2^+.
[f] For a pure water ice surface in Saturn's magnetosphere, using model of Teolis et al. (2010b).
[g] Taken to be constant in time. Given by Avg in-flight Abundance times Total Loss Rate.
[h] Global average over all ions and energies, using ambient plasma surface ion bombardment fluxes from Teolis et al. (2010b).
[i] Treats sputtering by ions as the dominant source process as Teolis et al. (2010a) found for pure water ice. Even lower (ion) sputtering yields result if photo, electron or micrometeoritic impact driven production/desorption contributions from the lag layer are appreciable.

estimated production and loss rates in Tables 2–3 represent global (spatial) and temporally averaged values as described in the Appendix.

Molecules were allowed in the model to transiently stick on returning to the surface, and were then either (1) desorbed at the local surface-temperature dependent vapor pressure (given by an Arrhenius law) with a cosine thermalized (Maxwellian) velocity distribution, (2) re-sputtered back into the atmosphere, or (3) diffused into the subsurface regolith. We implemented subsurface gas and thermal diffusion by numerically solving Fick's law versus time (diurnally and seasonally) and depth, over a global 200/100 latitude / longitude grid, taking into consideration the gas and thermal diffusion coefficients, and the surface gas and solar heat source. We calculated the solar source as the cosine of the local solar zenith angle, including the local time (diurnal) dependence, and the seasonal variability of the solar declination (+/– 26.73°). The thermal diffusion coefficient is equal to $(I/\rho/C)^2$, where I, ρ, and C are the ice regolith thermal inertia, heat capacity and mass density (Howett et al., 2010), while that of the gas was set to $L^2/(2(\tau_s+\tau_f))$, with L the inter-grain spacing (set to 3 microns, in the range inferred from IR reflection spectra (Scipioni et al., 2014, 2013)), τ_f the molecule flight time between grains, and τ_s the sticking time on a grain (Schorghofer and Taylor, 2007). The thermal model yields Dione(Rhea) equatorial max/min day/night surface temperatures of 55/95(~94/52) K, and polar max/min summer/winter temperatures of 83/25(81/22) K, consistent with Cassini Infrared Spectrometer temperature data (Howett et al., 2014; Howett et al., 2010; Howett et al., 2016). All simulations were run over several Saturn seasonal cycles to achieve an approximate long-term steady-state solution. Since we do not include (negligible) 'non-linear' exospheric drivers like intermolecular collisions and (as discussed later) secondary sputtering, the model exosphere scales proportionally to the input total source rate. Therefore at the end of the simulations we scaled (Figs. 2, 3, 6 and 8) the O_2 and CO_2 source rates to best match the densities

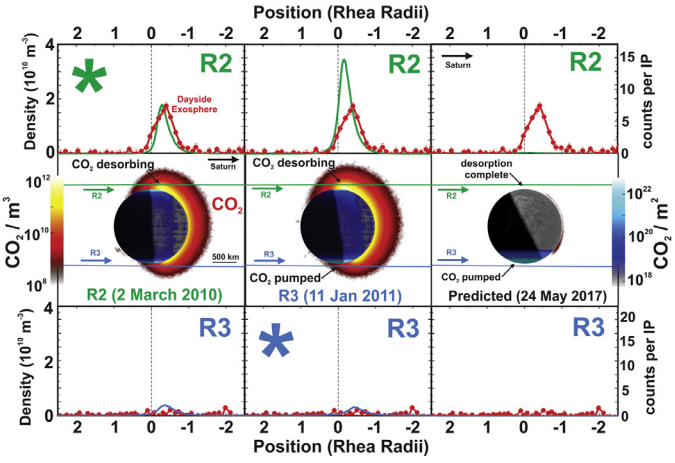

Fig. 2. Rhea CO_2 exospheric model results, showing (center row) the surface solar illumination (dawn terminator as viewed over the equator), and predicted gas density cross sections and surface frost column density at the R2 (left) and R3 (center column) flyby dates and times, and prediction (right) for the 2017 Saturn solstice. (Top) Comparison of the observed (red points, data binned) and predicted (green line) CO_2 densities versus position from closest approach along the R2 trajectory (x-axis, in Rhea radii, dashed line: closest approach). (Bottom) Same for the R3 flyby trajectory. Asterisks denote model-data comparisons with the same flyby date; all other plots show model projections to different dates. We assumed a 3.7×10^{21} CO_2/s source rate as required to match the observed peak density on both flybys. The observation of CO_2 concentrated on the dayside is consistent with the modeled exospheric structure due to night side and polar cryopumping. CO_2 was desorbing from the north, and cryopumping onto the southern polar surface during the flybys. Accordingly, as anticipated by the model (bottom center), CO_2 was undetectable in the south on R3. As shown (right) exhaustion of the northern frost cap should result in the collapse of the CO_2 exosphere by the time of the 2017 solstice. (For interpretation of the references to colour in this figure legend, the reader is referred to the web version of this article).

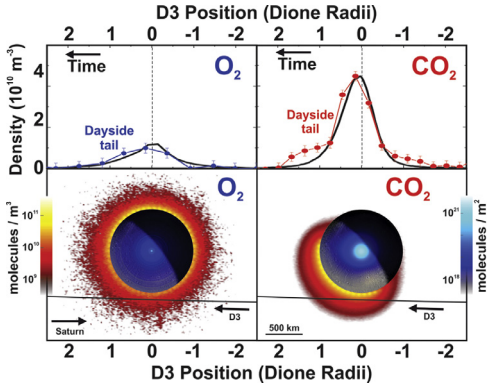

Fig. 3. Dione O_2 (left) and CO_2 (right) exospheric model results, showing (bottom) the surface solar illumination (north polar view), and predicted equatorial gas density cross sections and surface frost column density at the 12 Dec 2011 D3 flyby date and time. (Top) Comparison of the observed (blue points: O_2, red points: CO_2, data binned) and predicted (black lines) O_2 and CO_2 densities versus position from closest approach (dotted lines) along the D3 trajectory (*x*-axis, in Dione radii). We assumed 45 and 1.6×10^{21} s^{-1} O_2 and CO_2 source rates, as required to match the observed peak density, and applied Rhea's optimal surface interaction parameters (regolith diffusion with 0.11 and 0.25 eV O_2 and CO_2 sublimation energies). CO_2 and, to a lesser degree O_2, are concentrated over the dayside as predicted by the model. As observed at Rhea, the Dione exospheric model predicts seasonal exospheric variability (Fig. 7). (For interpretation of the references to colour in this figure legend, the reader is referred to the web version of this article).

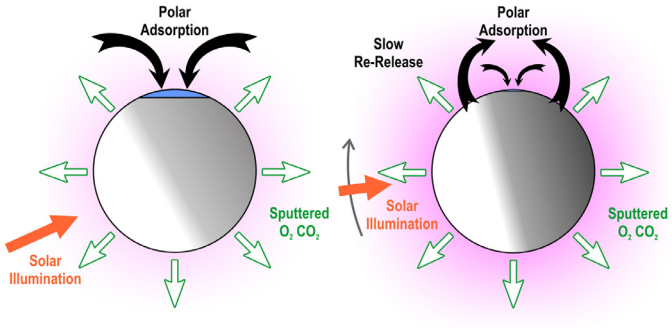

Fig. 4. Schematic showing the mechanism responsible for the exospheric seasonal variability. The exosphere is cryopumped at the solstices onto the cold winter polar surface. As equinox approaches the Sun rises over the winter latitudes, warming the surface and desorbing the frost cap to produce a transient augmentation of the exosphere.

detected by INMS, on the dates, times and trajectories along which they were measured.

The seasonal evolution of the model CO_2 exosphere is shown in Figs. 2 (Rhea) and Figs. 3 and 6 (Dione) during the times of Cassini's encounters, where we have assumed a 0.26 eV CO_2 sublimation energy (Giauque and Egan, 1937) and a constant global CO_2 surface source of 3.7×10^{21} molecules/s (Table 4). Exospheric CO_2 easily sticks to the night sides of both moons as seen in Figs. 2 and 3, but at low latitudes the body's rotation transports adsorbed CO_2 within half a day across the dawn terminator where it desorbs. However near the solstices the CO_2 also condenses at winter polar latitudes, and any CO_2 newly generated during this time becomes stuck (for years) near the winter pole within a few random walk hops over the surface. Hence the winter polar zone cryopumps the entire global exosphere and, e.g., the gas density is suppressed even over the opposite summer polar zone. Approaching the equinoxes the CO_2 gradually desorbs as the solar terminator advances poleward over the accumulated winter frost cap. The desorbed CO_2 supplies a transient exosphere over the dayside hemisphere and migrates to the opposite pole where it sticks again. A few years past equinox the CO_2 completes the transition between

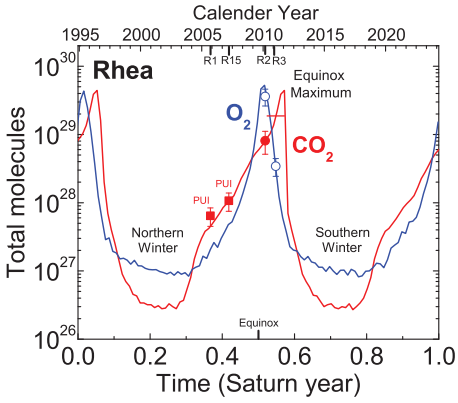

Fig. 5. Rhea modeled total O_2 (blue) and CO_2 (red) exospheric molecular abundance versus time over a Saturn season, showing the periodic exospheric maxima and minima at the equinoxes and solstices, respectively. The INMS (circles) and CAPS IMS (squares) abundances are extrapolations obtained by scaling the model exosphere (with predicted spatial structure at the flyby dates and times) to the measurements. Red dash: CO_2 upper limit from R3. The CO_2 frost cap has greater longevity than that of O_2, and therefore the CO_2 exospheric abundance peaks later in time. (For interpretation of the references to colour in this figure legend, the reader is referred to the web version of this article).

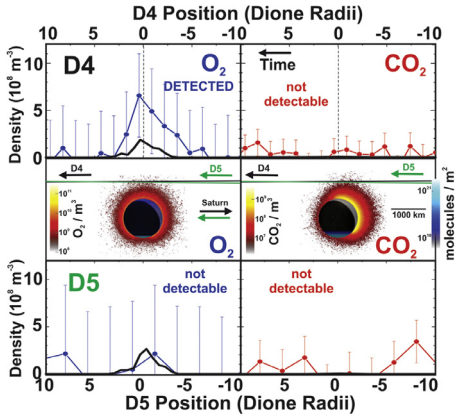

Fig. 6. Dione exospheric model used to fit the 12 Dec 2011 D3 data, projected out to the 16 Jun 2015 D4 and 17 Aug 2015 D5 flyby dates and times. (Top) Comparison of the observed (blue points: O_2, red points: CO_2, data binned) and predicted (black lines) D4 O_2 and CO_2 densities versus position from closest approach along the D4 trajectory (x-axis, in Dione radii). As predicted INMS detected O_2 but did not find CO_2, due to the collapse of the CO_2 exosphere between D3 and D4. The measured O_2 density is somewhat higher than expected by a factor 2–3, possibly due to the heightened exospheric sensitivity to magnetospheric variations as solstice approaches. (Bottom) Same comparison for D5. INMS did not detect either species at D5 outside the noise. (Center) Exospheric O_2 and CO_2 model cross sections (equatorial viewpoint, dawn terminator at right) at the D4 flyby date and time: the model is little changed by D5 only 2 months later. Trajectories are drawn consistently with the flyby local time, and are roughly perpendicular to the viewpoint shown. (For interpretation of the references to colour in this figure legend, the reader is referred to the web version of this article).

poles, and the atmospheric density rapidly collapses in ~1 (Earth) year. The phenomenon repeats (Fig. 4), forming a transient dayside atmosphere around every equinox, i.e., every 14.7 years, in a seasonal polar volatile migration cycle roughly analogous to those observed at Triton (Buratti et al., 2011) and Pluto (L A Young, 2013). The R2, R3 and D3 flybys occurred shortly (0.02, 0.05, and 0.08 Saturn years) after northern spring equinox during the period when the predicted exospheric densities are maximal.

The CO_2 model yields good agreement with the Dione and Rhea data as shown in Figs. 1–3, matching both (1) the skew of the density profiles toward the dayside portion of Cassini's trajectories, and (2) the variability between flybys; particularly as seen between the northern and southern R2 and R3 encounters.

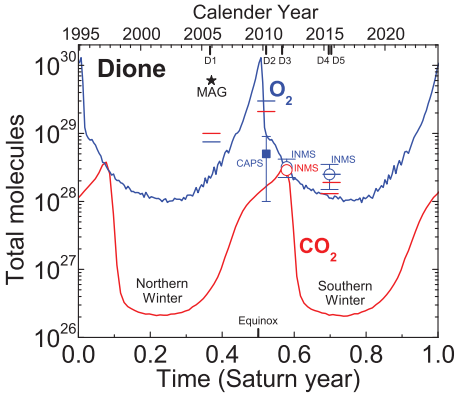

Fig. 7. Dione modeled total O_2 (blue) and CO_2 (red) exospheric molecular abundance versus time over a Saturn season, showing the periodic exospheric maxima and minima at the equinoxes and solstices, respectively. The INMS (circles) abundances are extrapolations obtained by scaling the model exosphere (with predicted spatial structure at the flyby dates and times) to the measurements. We also show (square) the CAPS IMS O_2 estimate of Tokar et al. (2012), with their ionization rate scaled to our rate obtained from Table 3. Dashes: INMS upper limits for O_2 (blue) and CO_2 (red). The magnetometer based molecular abundance (star), from Simon et al. (2011), exceeds the INMS upper limits (see text). (For interpretation of the references to colour in this figure legend, the reader is referred to the web version of this article).

Remarkably, despite the lack of CO_2 during R3 (Fig. 2), the model exospheric CO_2 global abundance was in fact still rising (Fig. 5) at the times of the R2 and R3 flybys. Hence the CO_2 non-detection on R3 is not attributable to the exosphere's temporal variability according to the model, but is rather indicative of its spatial structure. While the north was a sublimation source of the previous winter's CO_2, the south (depleted of CO_2) was coming out of summer, and was therefore beginning to cryopump CO_2 out of the exosphere. Therefore the gas source was concentrated in the north at the times of the encounters. At Dione the northern latitudes were still outgassing significant CO_2 during the 2011 D3 encounter (Fig. 3), which is consistent with the dayside CO_2 detection during this equatorial flyby. By contrast the 2015 D4 and D5 flybys 2.5 (Earth) years later occurred after the Dione northern CO_2 source was exhausted (Figs. 6–7), explaining the lack of detection of CO_2 (in contrast to O_2 at D4, Fig. 1b) during these flybys.

The model Dione and Rhea O_2 exospheres (Figs. 3 and 8) also exhibit seasonal variability, but the spatial structure is more uniform than that of CO_2, with the O_2 more evenly distributed between north and south and the day and night sides. Contrary to CO_2 the more volatile O_2 molecules are not stuck onto the night side surface except at the winter polar latitudes where surface temperatures approach 20 K. The exosphere is thermally equilibrated with the local surface temperature since O_2 molecules jump ballistically an average of only 300(230) km at a time across Dione's (Rhea's) surface; significantly less than the 1123(1528) km diameters of these bodies. Accordingly, the model O_2 exosphere only exhibits a difference of scale height between the day and night sides, which is consistent with the weak day/night O_2 asymmetry observed at R2 (Figs. 1 and 8). Unlike CO_2 the drop in O_2 between R2 and R3 is difficult to intepret in terms of spatial structure, since (despite O_2 desorption from the north at the times of the flybys) the southern terrain was still too warm (~35 K) to efficiently remove O_2 from the southern exosphere. Rather, as shown in Fig. 8, the O_2 drop is consistent with a temporal change; a rapid collapse in Rhea's entire O_2 exosphere in the 10 months between R2 and R3, due to the completion of gas sublimation from the north during this period. The exhaustion of the model's northern polar frost supply occurs earlier for O_2 than the less volatile CO_2, and (unlike CO_2) before the south is cold enough to pump exospheric O_2.

Surface sticking drastically lengthens the average molecule residence time in the system; our exosphere models suggest O_2 and CO_2 at Dione(Rhea) to be ~3(3) and ~160(700) Earth years old, including time adsorbed and in flight. Near equinox we estimate that ~99% of the Dione and Rhea exospheric O_2 and CO_2 is attributable to polar desorption of molecules from prior seasons, and therefore the exospheres are insensitive during equinox to transient changes of the molecule source rates, e.g., from magnetospheric fluctuations leading to time variability of surface sputtering. However the recent Dione D4 and D5 flybys sampled (Fig. 1b) the O_2 exosphere

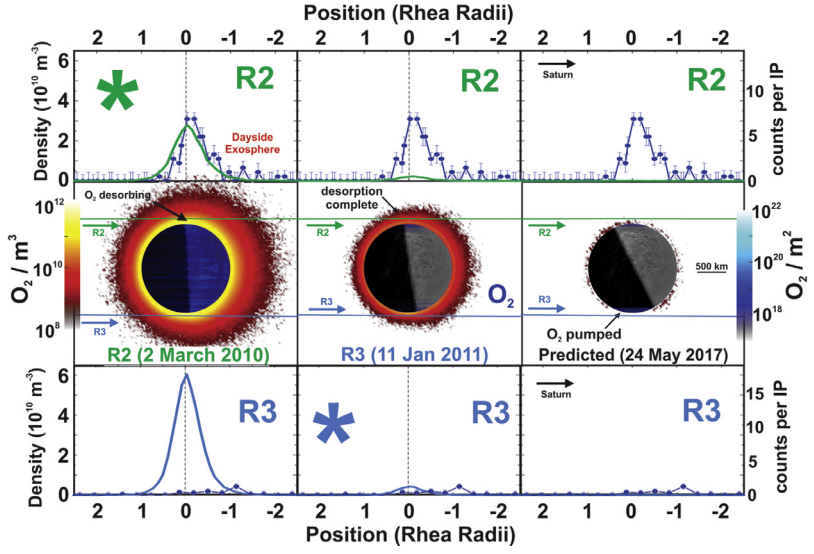

Fig. 8. Rhea O_2 exospheric model results, showing (center row) the surface solar illumination (dawn terminator as viewed over the equator), and predicted gas density cross sections and surface frost column density at the R2 (left) and R3 (center) flyby dates and times, and prediction (right) for the 2017 Saturn solstice. (Top) Comparison of the predicted (green line) and observed (red points, data binned) O_2 densities versus position from closest approach along the R2 trajectory (x-axis, in Rhea radii, dashed line: closest approach). (Bottom) Same for the R3 flyby trajectory. Asterisks denote model-data comparisons with the same flyby date; all other plots show model projections to different dates. We assumed a 7.2×10^{21} O_2/s source rate as required to match the observed peak density on both flybys. An O_2 tail is detected on the dayside, consistent with the anticipated greater dayside scale height. Unlike CO_2, the southern latitudes are not yet cold enough to cryopump O_2 from the southern exosphere on the R2 and R3 flybys dates. However, the modeled O_2 frost cap is exhausted between the R2 and R3 flybys, resulting in an anticipated collapse of the global exosphere, consistent with the reduced O_2 detection on R3.

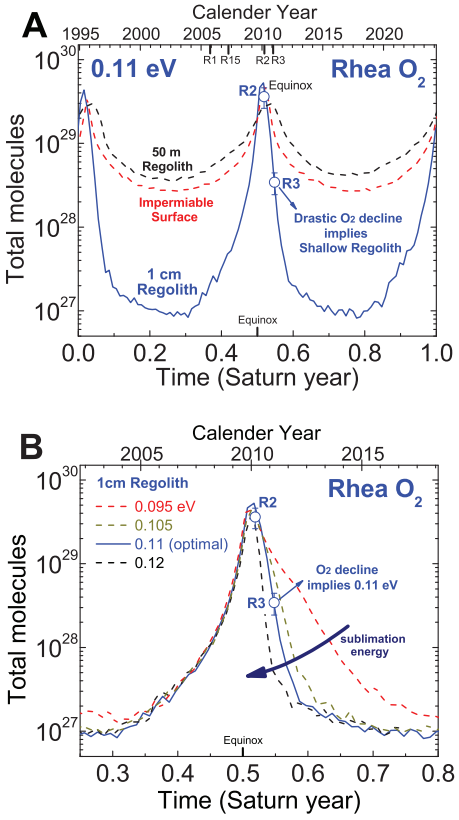

Fig. 9. Modeled Rhea exospheric O_2 molecular abundance versus time with different assumptions for regolith diffusion and sublimation energy. (A) The cases of deep (50 m) regolith diffusion (dashed, black line), and no diffusion (dashed, red line), both under-estimate the sharp exospheric decline between R2 and R3. However the shallow (1 cm shown) regolith model correctly anticipates (solid line) the decline. (B) Model result with difference assumptions for O_2 sublimation energy. (For interpretation of the references to colour in this figure legend, the reader is referred to the web version of this article).

near solstice during which polar desorption is minimal, and the exospheres consist nearly entirely of newly created molecules which have not yet stuck to the winter latitudes. Hence the solstice gas densities are more responsive to magnetospheric variations, with time constants of order ~1 Earth day, and such variability may explain the finding at D4 of O_2 densities 2–3 times greater (Fig. 6) than predicted by the exospheric model (which assumes a constant magnetosphere). However, despite the non-detection of O_2 at D5 (Fig. 1b), we cannot infer (outside error) variability in O_2 between D4 and D5. INMS was less sensitive (by ~50%) at D5 due to the higher ram angle (Teolis et al., 2015), 68° versus 42° at D5 versus D4, and therefore it's possible (within the D5 error bars, Fig. 6) that the O_2 exosphere did not change between flybys.

We used the exospheric O_2 collapse from R2 to R3 to constrain the gas–surface interaction, i.e., molecule sublimation energy and the role of regolith diffusion. As shown in Fig. 9A for O_2, the extreme cases of (1) diffusion into a deep regolith (50 meters), or (2) no regolith diffusion (i.e., an impermeable non-porous surface), both under-estimated the exospheric collapse, but for different reasons. For a deep regolith polar O_2 migrates into the depth when the winter frost cap comes back into sunlight, then slowly diffuses back up to the surface and outgasses, maintaining the exosphere long past equinox. For an impermeable surface the frost cap is exposed to the magnetospheric plasma which sputters it back into the exosphere, thereby lessening the exospheric seasonal variation. However the shallow regolith case with permeability no more than a few meters yields agreement of the model O_2 exosphere with the observed exospheric O_2 collapse (Fig. 9A). In this case polar regolith diffusion times are short ('instantaneous' within the 150 s simulation time step), but the adsorbed molecules are nonetheless dispersed into the near-surface regolith, shielding them against re-sputtering from the top surface.

We also found (Fig. 9B) that an adjustment of the O_2 sublimation energy to ~0.11 eV is required to reproduce the steepness of the observed O_2 exospheric collapse; slightly above the 0.095 eV (Rook et al., 1985) implied by the vapor pressure of pure solid oxygen. Hence the O_2 is slightly less volatile than expected, which may be indicative of the state of the surface material, e.g., the degree of surface chemical activation by solar UV and/or magnetospheric particle bombardment. Evidence for a similar effect is seen at Mercury, where Cassidy et al. (2015) have suggested that surface activation (Yakshinskiy et al., 2000) by space weathering may explain the non-detection of a thermalized exospheric sodium source. We note that O^- PUIs detected on R1 by the CAPS Electron Spectrometer (ELS) (Teolis et al., 2010a) appear to emanate from the surface, as inferred from (1) the insufficiency of gas phase dissociative electron attachment cross sections (Itikawa, 2008) to account for the observed O^- flux from gaseous O_2 at altitude, and (2) the backtracked O^- trajectories which 'focus' onto the night side surface (see Fig. 2A in (Teolis et al., 2010a)). This suggests a surface mediated process, such as dissociative attachment reactions with O_2 adsorbed on the night side (Tang et al., 1996), but further study is needed to elucidate the reaction and the relation to the state of Rhea's surface (which may be coated by a carbonaceous lag layer, see below).

Our analysis (Figs. 10–11) of the CAPS Ion Mass Spectrometer (IMS) (Young et al., 2004) ion energy-time spectrograms in anodes 3 (R1) and 7 (R1.5)—which had the most intense PUI signals—also indicates composition, seasonal evolution and spatial structure consistent with the INMS-based exospheric modeling. We backtracked the PUI common cycloid trajectories from the anode FOV in Cassini's reference frame, considering 24 nT and 1.4 V/km magnetic and co-rotation electric fields (Roussos et al., 2008; Teolis et al., 2014), and excluding PUI trajectories that originate within or strike the body. We then compared the approximate PUI zone of origin near Rhea (the sampling zone, lying at the cycloid cusps) against the predicted exospheric density and structure by projecting the exospheric model (fit to INMS) back to the dates and times of the CAPS measurements. Finally we integrated across the sampling zone, and scaled by the ionization rate (Tables 3–4), to obtain the predicted PUI signature versus time; finding that the timing, intensity and shape of the observed signatures were consistent with CO_2^+ rather than O_2^+ ions as shown in Fig. 10. The R1 PUI signature cuts a cross section of the dayside CO_2 exosphere, roughly approximating the exospheric density versus altitude down to the surface (at ~–350 s). The signature also shows the expected deficiency of CO_2 on the night side, as can be seen after comparing against the uniform exosphere case (Fig. 10). For the ten times more distant R1.5 flyby, the projection of the anode's 8.5° FWHM elevation angular acceptance back to Rhea yields a 3D sampling box with significant thickness out of the gyroplane (Fig. 11), which must be considered if the PUIs acquire out-of-plane velocity components by scattering (thermalization) with the ambient plasma. We integrate the model exosphere over this 3D box to approximate the expected PUI signal, and predict a double-peaked PUI signature as also observed by CAPS. These two peaks appear to correspond to the dayside CO_2 exosphere, and the localized CO_2 source from the northern frost cap, as shown in Fig. 11. Overall, the CAPS based global CO_2 abundances show a ~50% increase from R1 to R1.5 (Fig. 5) consistent with the anticipated exospheric build-up toward equinox. Also as expected the CAPS abundances (from 2005 to 2007) are a factor ~10 below those later observed by INMS in 2010–2011 during northern spring. One can see in Fig. 5 that the

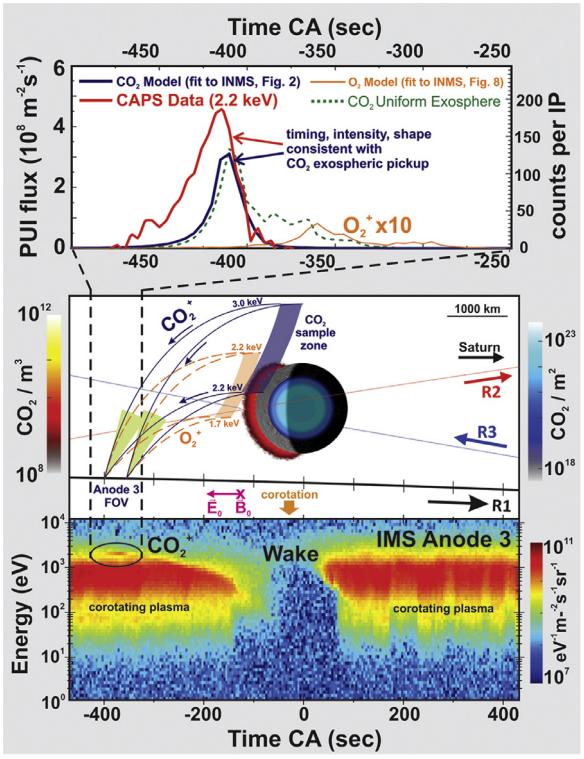

Fig. 10. Comparison of the Rhea pickup ion flux and distribution detected by CAPS IMS anode 3 on the R1 flyby, to that anticipated by the model CO_2 and O_2 exospheres, fit to the later INMS R2 and R3 data and projected back to the R1 flyby date and time. (Bottom) Anode 3 ion flux energy spectrogram with the PUI signature circled. The flux calculation is given in the CAPS user's guide (Wilson et al., 2012): efficiencies vary ~+/15% between ion species (we used the O_2^+ efficiency (Tokar et al., 2012) as CO_2^+ values are not available). Contrary to the sharp energy signature of the fresh PUIs which follow only common cycloid trajectories, ambient corotating ions have a broad energy distribution since they enter the anode along thermalized prolate and curtate cycloids. (Center) R1 flyby configuration showing the Rhea exospheric CO_2 density cross section, Rhea surface illumination and adsorbed column density, the region (purple: CO_2^+, orange: O_2^+) sampled by anode 3 during the PUI detection, the anode 3 FOV at the time and location of the PUI detection along the R1 trajectory, and the limiting O_2^+ and CO_2^+ energies (on arrival at Cassini) and trajectories accepted into anode 3. We approximate the R1 sampling region as 2D in the flyby's equatorial plane. (Top) Anticipated (dark blue: CO_2^+, orange: O_2^+ scaled times ten) and measured (red) total PUI signal versus time from closest approach, compared to the expected profile (dashed line) for a uniform CO_2 exosphere. As shown the timing, intensity and shape of the signal is not consistent with O_2^+ (nor with fragments such as CO^{n+}, O^{n+}, C^{n+}), but is consistent with CO_2^+. The absence of a shoulder after −350 s is consistent with a dayside exosphere, as anticipated by the CO_2 exosphere model and later observed by INMS. (For interpretation of the references to colour in this figure legend, the reader is referred to the web version of this article).

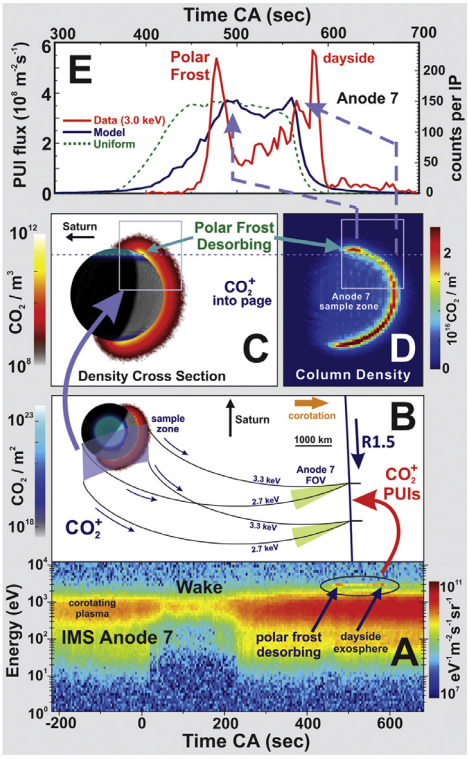

Fig. 11. Comparison of the Rhea pickup ion flux and distribution detected by CAPS IMS anode 7 on the R1.5 flyby, to that anticipated by the model CO_2 exosphere (fit to the later INMS R2 and R3 data) projected back to the R1.5 flyby date and time. (A) Anode 7 ion flux energy spectrogram with the PUI signature circled. (B) R1.5 flyby configuration showing Rhea with the model exospheric CO_2 density cross section and adsorbed column density, the surface illumination, the region (purple box: CO_2^+) sampled by anode 7 during the PUI detection, the anode 7 FOV at the time and location of the PUI detection along the R1.5 trajectory, and the limiting CO_2^+ energies (on arrival at Cassini) and trajectories accepted into anode 7. (C) Equatorial view of the model exosphere viewed through the sample box, showing the box's approximate north–south extent if the anode 8.5° FWHM elevation angular acceptance is projected back to Rhea. (D) Exospheric column density from the orientation of (C) as sampled by anode 7, showing the intense feature from polar frost desorption. (E) Anticipated total anode 7 PUI signal versus time from closest approach (red), with arrows showing the correspondence of the double peaked structure to the polar frost desorption, and dayside exospheric signatures seen in (D). As at R1 (Fig. 10) the timing, intensity and shape of the signal is not consistent with O_2^+ (not shown) nor fragment species, but is consistent with CO_2^+. The observed PUI signature (red) shows a similar (even more intense) double peaked structure, which implies that CAPS is observing a CO_2 exosphere with abundance and spatial structure consistent with INMS based modeling. For comparison we also show (top, dashed line) the expected PUI profile for a uniform CO_2 exosphere. (For interpretation of the references to colour in this figure legend, the reader is referred to the web version of this article).

CO_2 model exospheric abundance, plotted versus time, is consistent with the changes over time implied by CAPS and INMS.

We have also estimated exospheric upper limits from the Dione D1 and D2 flybys in Fig. 7 by comparing the expected (modeled) gas distribution at Cassini's altitude and trajectory against the INMS detection limit (given by species sensitivity, background signal, binning resolution, and instrument pointing). The analysis is not suitable for all flybys: in particular the Rhea R1 and R4 (Table 1) INMS data fails to give useful upper limits due to the altitude and poor instrument pointing. The D1 pointing was fortuitous: despite the high 77 degrees ram angle of the INMS gas inlet, the instrument's venting aperture (see (Teolis et al., 2015)) was aimed only 24° from ram, which should have allowed detection by INMS of the exosphere estimated at D1 from MAG (Simon et al., 2011). However as shown in Fig. 7 the non-detection of gas by INMS at D1 sets upper limits of $1(0.8) \times 10^{29}$ $O_2(CO_2)$ on Dione's exosphere almost an order of magnitude below MAG. A possible contributing factor to the MAG result may be the passage of the D1 trajectory near the edge (0.93 Dione Radii from the center) of the southern flux tube. MAG also detected Rhea flux tube field perturbations during the R2 and R3 flybys, but these are strongly influenced by Rhea's flux tube thermoelectric current system, formed to balance ion and electron currents onto the surface (Teolis et al., 2014). While a global Dione exosphere below the limit set by INMS at D1 should have been undetectable by MAG, it's possible a flux tube current at Dione similar to Rhea's may have contributed to the magnetic field signatures seen during the D1 flyby. Alternatively, non-volatile molecules from a localized gas source below Dione's 0.51 km/s escape velocity, such as an Enceladus-like water plume, would stick permanently on falling back to the surface, and may thereby have evaded detection by INMS if located in the (northern) hemisphere opposite to the flyby. However further investigation is

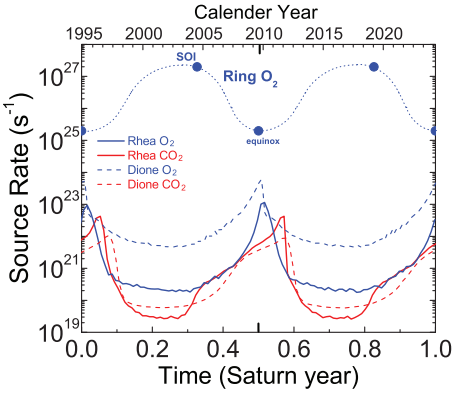

Fig. 12. Dione and Rhea O_2 and CO_2 total exospheric loss rates, estimated by scaling the model exospheric abundances (Figs. 5 and 7) to the total O_2 and CO_2 loss rates (Table 4) compared to (blue circles) the ring O_2 source rate from Tseng et al. (2013) (dotted line to guide the eye). We estimate (Table 4) that ~83(59)% of O_2, and 71(10)% of CO_2 lost from Dione(Rhea) escapes gravitationally to supply Saturn's magnetosphere with neutral O_2 and CO_2, while ~8(18)% and ~13(41)%, respectively, is converted to O_2^+ and CO_2^+ PUIs. Additionally from Table 3 we estimate the conversion factors of O_2 to O^+, O^{++}, and O to be –2(5), 0.1(0.2) and 17(37) %, where the negative 2% Dione O^+ value represents net removal of magnetospheric O^+ by charge exchange with O_2 (Table 3, loss channel 1). We note that Dione and Rhea should also be non-seasonal sources of sputtered gravitationally escaping H_2O and radiolytic H_2 (Teolis et al., 2010b). The ring O_2 source has opposite seasons to the icy satellites, peaking at the solstices rather than the equinoxes. (For interpretation of the references to colour in this figure legend, the reader is referred to the web version of this article).

needed to evaluate the compatibility of INMS detection limits for such a source with the MAG data.

3. Discussion

The Dione and Rhea seasons are the temporal inverse of Saturn's photo-desorbed ring O_2 source, which depends on the ring plane angle to the Sun, and peaks at the solstices (Christon et al., 2013; Elrod et al., 2014; Tseng et al., 2013) rather than the equinoxes. Even assuming constant sputtered O_2 and CO_2 sources from Dione and Rhea as done by our modeling, the seasonality of the exospheric gas densities results in a variable supply of species to the magnetosphere which is 'out of phase' (Fig. 12) with the ring source. However the ring O_2 source is in the range $\sim 10^{25}$–10^{27} O_2/s (Tseng et al., 2013), dwarfing that of Dione and Rhea (Table 4), and even at the equinoxes we estimate the ring O_2 source to be roughly two orders of magnitude above that of Dione and Rhea (Fig. 12). Therefore Saturn's magnetospheric O_2/O_2^+ density and variability should have a predominantly ring origin, except possibly (near equinox) at Rhea's L-shell (Martens et al., 2008). The CO_2^+ PUI source from Dione and Rhea to the magnetosphere also exhibits a weak ~+/–15% diurnal variability depending on the moon's orbital position, as PUIs from the dayside exosphere are blocked by the body when the sunlit hemisphere is Saturn facing. Saturn's other massive icy satellites Tethys and Mimas, located closer to the planet at 4.9 and 3.1 R_S, may also be seasonal/diurnal exospheric sources of species to the magnetosphere. Although Cassini's mission does not take the spacecraft close enough to Tethys or Mimas for exospheric measurements, the understanding gained from Dione and Rhea can inform future exospheric estimates and models at Saturn's other icy satellites.

The estimated O_2 source rates of 45 (Dione) and 7.2 (Rhea) $\times 10^{21}$ s^{-1} are factors of ~50 and 300 below the predicted values of ~2.1 and 2.2 $\times 10^{24}$ s^{-1} from radiolysis/sputtering of water ice, after accounting for published (Table 3, right column) flux/energy spectra of magnetospheric particles and solar UV incident onto the Dione and Rhea surfaces, and laboratory radiolytic oxygen yields from ice at the relevant temperatures as analyzed by Teolis et al. (2010b). The discrepancy may be indicative of surface composition alteration by preferential sputtering and escape of the light and/or volatile surface constituents and radiolysis products, leaving a surface refractory lag layer residue resistant to sputtering. One relevant process is preferential gravitational escape: e.g., ~90(83)% of sputtered H_2O molecules escape Dione(Rhea) gravitationally without re-impacting the surface (Teolis et al., 2010b). Also roughly half the surface H_2O may be converted to sputtered H_2 and O_2 molecules (Teolis et al., 2010b) which escape (along with CO_2) with near unity probability due to their volatility: either (1) gravitationally immediately on being ejected, or (2) over time from the exosphere. A water ice surface containing impurities is therefore enriched over time in refractory constituents with both (1) low sputtering yield (high sublimation energy), and (2) minimal volatile radiation products.

A major consequence of a refractory lag layer is the elimination of secondary sputtering ('self' sputtering by surface-impinging PUIs (Poppe et al., 2013)) as a significant exospheric contributor. The exospheric thickness is hundreds of km, sufficient for acceleration of O_2^+ and CO_2^+ PUIs to the local plasma convection speed (~40(Dione) and 50(Rhea) km/s), i.e., hundreds of eV (corresponding roughly to the ambient plasma temperature), prior to impacting the surface. The result for a pure water ice surface would be effective sputtering yields (i.e., globally averaged over all ions and energies) at Dione and Rhea of order unity or greater (Table 4), which would likely result (near the equinoxes) in a runaway feedback, i.e., the PUIs produce more exosphere, yielding more PUIs and so on, leading to a self-limiting exosphere of sufficient density to slow/impede the surface-impingent magnetospheric plasma (Cassidy et al., 2012). However the observed Dione(Rhea) sputtering yields are at least two orders of magnitude less than unity (Table 4), precluding their exospheres from achieving the self-limiting feedback state.

The significant proportion (Table 4) of CO_2 compared to O_2 supplying the Dione and Rhea exospheres (1:30 and 1:2 CO_2:O_2, respectively) may indicate radiolysis/sputtering from a lag layer enriched in carbon. The preponderance of CO_2 rather than CO in the radiolytic end products could then be driven by reactions involving H_2O: e.g. pure solid CO_2 yields ~100–1000 times more radiolytic CO than CO_2 (Raut and Baragiola, 2013), but H_2O dissociation into OH radicals (e.g., left behind by hydrogen escape from the surface monolayers (Teolis et al., 2009; Teolis et al., 2005)) allows for conversion of CO to CO_2 in barrierless near-surface CO + OH reactions (Petrik et al., 2014). Additional CO_2 sources may be cryovolcanism (though no evidence for such current activity at Dione or Rhea has yet been found), rapid destruction and conversion of exospheric CO through surface OH reactions (Yuan et al., 2014), or UV photosynthesis reactions of adsorbed O_2 with surface carbon (Fulvio et al., 2012). The low Dione and Rhea sputtering yields (Table 4) are actually on par with those of graphite (Lifshitz et al., 1990), which may imply CO_2 radiolysis at the interface of water ice under a graphitic lag layer (Raut et al., 2012; Shi et al., 2015; Sabri et al., 2015) and/or radiolytic CO_2 evolution from a surface graphitic oxide layer (Hou et al., 2015; Matsumoto et al., 2011). However fresh H_2O deposition by ice rich E-ring grains, and lag layer destruction by E-ring grains and micrometeorite impact gardening also ensures continual exposure on a fraction of the surface material of freshly deposited/upturned H_2O to irradiation, thereby ensuring a radiolytic O_2 source to the exosphere. The micrometeorites may simultaneously re-supply carbon into the surface which can be incorporated into radiolytic CO_2 when the lag layer reforms over the impact site (Clark et al., 2008; Cruikshank et al., 2010). Finally impact vaporization contributes to the release of trapped radiolytic O_2 and CO_2 into the exosphere. Accordingly, impact-driven deposition/gardening/ejection may be the limiting factor (Killen et al.,

2004) on the source rates of at least one (O_2), and possibly both major exospheric species.

A sputter-produced lag layer may be only angstroms thick, i.e., the topmost surface monolayers from which radiolysis products escape; too thin for detection in the visible-infrared solar reflection spectrum by the Cassini Visible and Infrared Mapping Spectrometer (VIMS) which is sensitive to micron thicknesses given by regolith grain size (Stephan et al., 2012; Stephan et al., 2010). However impact gardening mixes lag layer constituents down to micron depths visible to VIMS, possibly contributing to the low albedo (Cruikshank et al., 2005) non-ice constituents seen in the IR spectra of the Dione and Rhea trailing hemispheres where maximal sputtering occurs (Ciarniello et al., 2011; Stephan et al., 2012; Stephan et al., 2010). Surface CO_2 detected by VIMS at Dione (Scipioni et al., 2013; Stephan et al., 2010), and recently at Rhea (Scipioni et al., 2014; Stephan et al., 2012), is likely trapped in the surface ice (e.g. radiolytic CO_2 mixed down from the lag layer), and has probably not yet been ejected into the exosphere, as VIMS cannot see the exospheric CO_2 adsorbed onto cold polar and night side terrains not in sunlight. A refractory lag layer also blocks sputtering of radiolytic oxidants from the surface material, possibly enabling accumulation of sufficient trapped CO_2 and O_2 for synthesis of ozone (Teolis et al., 2006), as identified by Noll et al. (1997) in the surfaces of Dione and Rhea from Hubble Space Telescope UV spectra.

We can estimate the (globally averaged) carbon content of Dione and Rhea's 'bulk' surface material below the lag layer, i.e., within the gardened regolith, from the stoichiometric composition of the exospheric source material. For the stoichiometric calculation we include ejected H_2O and radiolytic H_2; both undetectable by INMS due to rapid gravitational escape and, for H_2O, permanent re-adsorption of molecules falling back to the surface. We assume an H_2O source roughly equal (Teolis et al., 2010b) to O_2's (Table 4), and equate H_2 to the number of O atoms in O_2 and CO_2, i.e., stoichiometrically consistent with an origin of most H and O from bulk H_2O (yielding from Dione (Rhea) $9.3(2.2) \times 10^{22}$ H_2/s). With the relative CO_2:O_2 source rates inferred here from exospheric observations (Table 4), we obtain a bulk Dione(Rhea) surface composition containing 0.01(0.13) C atoms per H_2O molecule. These compositions are presumably a combination of water and organics both endogenous to Dione and Rhea, and deposited by E-ring grains and micrometeorites. The dilution of Dione's estimated carbon fraction compared to Rhea's may reflect differing H_2O deposition rates by ice-rich E-ring grains, which are ten times more numerous at Dione than Rhea (Srama et al., 2011).

4. Implications

The Cassini spacecraft's traversals and in situ sampling of the O_2 and CO_2 exospheres of Dione and Rhea, and the discovery of exospheric structure and seasons, have transformed the understanding of radiolytic exospheres at icy planetary bodies. The combination of direct exospheric sampling by INMS with ionization/escape rate observations from CAPS PUI measurements has yielded two key discoveries: that (1) implied radiolytic O_2 source rates are well below [by factors ~50(Dione) and 300(Rhea)] those expected from radiolysis/sputtering of pure water ice by Saturn's plasma, and (2) surface interactions (adsorption/diffusion) appear to control exospheric structure and variability. The exospheric time evolution implies diffusion into a porous regolith at Dione and Rhea, which may occur by molecule adsorption/desorption between regolith grains. Accordingly, the seasonality may be maintained by polar frost dispersal into the regolith, where the frost is protected against re-sputtering back into the exosphere.

The consistency of the observations with O_2 source rates radically less than expected from a sputtered water ice surface in Saturn's magnetosphere, and the possibility of an oxygenated carbonaceous surface lag layer that is both (1) resistant to sputtering and (2) the possible CO_2 source, are findings of major significance for modeling and laboratory based estimates of surface composition and sputtering at icy objects, and of the source rates, densities, and compositions of their exospheres. Two potentially important implications of a refractory lag layer are (1) elimination of secondary sputtering and PUI-driven self-limiting feedback as salient exospheric processes, and (2) control of the exospheric source rates by impact driven deposition/gardening resulting in delivery of exogenous material, fresh ice exposure to radiolysis, and vaporization/release of radiolysis products.

The timing and locations of the Cassini flybys—across the terminator, and near equinox when the gas densities were detectable by INMS—were fortuitous, enabling direct observations of the species-dependent exospheric spatial and temporal variability, from only eight spacecraft flybys. The resulting discoveries at Dione and Rhea are a direct demonstration of the potential of low altitude spacecraft orbital or strategically placed/timed flyby trajectories, together with combined plasma and mass spectrometry measurements, to reveal exospheric origins and surface composition at other Solar System icy satellites such as Enceladus, Callisto, Ganymede, and Europa.

Acknowledgments

This research was supported by NASA and the Jet Propulsion Laboratory under SwRI subcontracts 1405851 and 1405853.

Appendix

In this Appendix we summarize the estimates of the exospheric loss rates from Table 3 for the electron and ion channels. The analysis of the magnetospheric energy distributions (used here to estimate interaction rates in the exosphere), is analogous to that also applied by Teolis et al. (2010b) at Rhea and Cassidy et al. (2013) at Europa, and in this work, to estimate O_2 sputtering from the surface. Neither the spatial nor temporal variability of the production and loss processes contribute significantly to the exospheric structure and dynamics due to the long molecular residence times (with the possible exception of solstice exospheric minimum, see text), and therefore the rates displayed in Table 3 are spatially and temporally averaged as described below.

We show in Figs. 13–15 the cross sections versus incident projectile energy for the 5 electron (electron impact and dissociative ionization (Itikawa, 2008)) and 14 ion channels (ion impact and dissociative ionization and charge exchange) of Table 3, where we

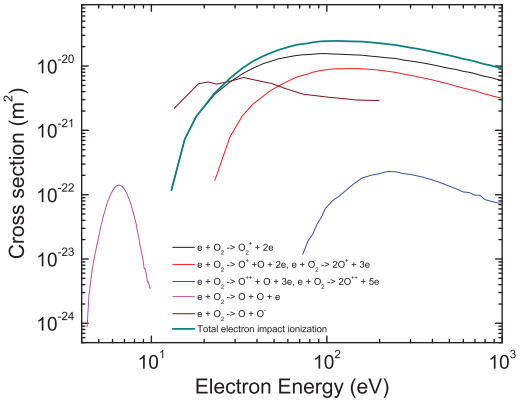

Fig. 13. Electron impact ionization and dissociation, and dissociative ionization and charge transfer cross sections, from Itikawa (2008), used to estimate the rates in Table 3.

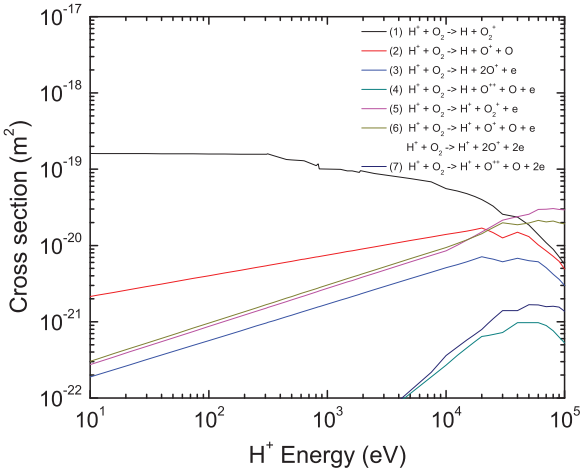

Fig. 14. H$^+$ impact ionization, charge exchange, and dissociative ionization and charge transfer cross sections with O_2 molecules used to estimate the interaction rates in Table 3. Data above 10 keV is from Luna et al. (2005). Based on the total charge transfer cross section measurements of Cabrera-Trujillo et al. (2004) and Williams et al. (1984), we extrapolated individual channels below 10 keV, see Appendix.

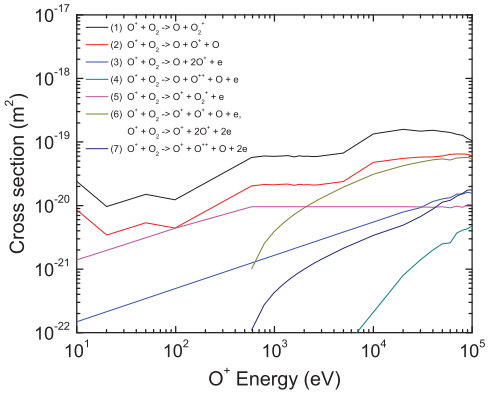

Fig. 15. O$^+$ impact ionization, charge exchange, and dissociative ionization and charge transfer cross sections with O_2 molecules used to estimate the interaction rates in Table 3. Data above 10 keV is from Luna et al. (2005). Based on the total charge transfer cross section measurements of Sieglaff et al. (2000), we extrapolated individual channels below 10 keV, see Appendix.

have used laboratory cross sections for H$^+$, and for O$^+$ (to approximate magnetospheric water group ions). We started with the data from Luna et al. (2005), which covers the 7 interaction channels numbered in the Figs. 14–15 legends for H$^+$ and O$^+$ with O_2 (14 channels total) from 10 to 100 keV. A difficulty with the Luna et al. (2005) ion data (unlike the electron data, Fig. 13) is that many of the cross sections do not peak in the measured 10–100 keV range. Although interactions above 100 keV can be neglected since most of the Saturnian plasma is below this energy, a major fraction of the plasma is below 10 keV. However laboratory data below 10 keV do not discriminate between the Luna et al. (2005) interaction channels, thus requiring extrapolations from the data which are available. For this purpose we used the (Sieglaff et al., 2000) total O$^+$–O_2 charge transfer cross sections from 0.01 to 10 keV, and H$^+$–O_2 transfer cross sections from (Williams et al., 1984) (2.5–25 keV) and (Cabrera-Trujillo et al., 2004) (0.3–2.5 keV). We applied our best judgment (described below) as to how these low energy cross sections are likely to be apportioned between the Luna interaction channels. We now briefly describe this process for H$^+$ (we applied similar reasoning to extrapolate the O$^+$ channels).

H$^+$ channels 2–7 decrease with energy, since they involve dissociation and ionization, and therefore consume kinetic energy from

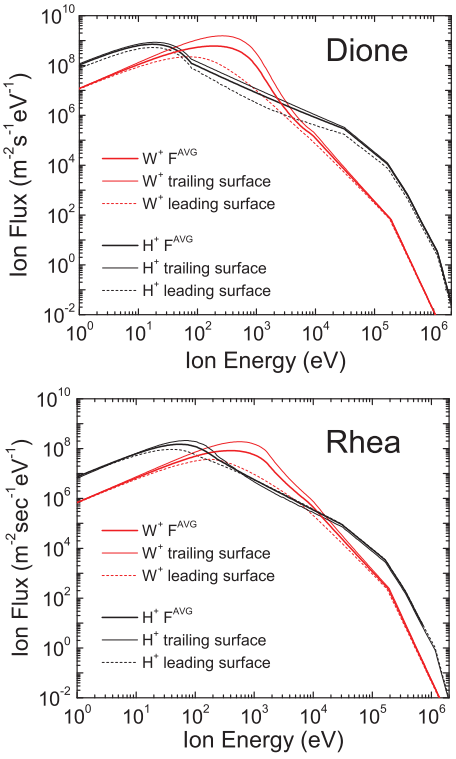

Fig. 16. The Dione and Rhea ion energy distribution functions estimated from the CAPS and MIMI based Saturn system survey studies of Dialynas et al. (2009), Thomsen et al. (2010), Wilson et al. (2008), Wilson et al. (2010). Bold lines (black: F_{H+}^{avg}, red: F_{W+}^{avg}) are the distributions spatially averaged around the body, which we used to estimate the Table 3 ion–O_2 interaction rates, as explained in the Appendix. For comparison we also show the distributions as seen at the surfaces of the leading and trailing hemisphere apexes. (For interpretation of the references to colour in this figure legend, the reader is referred to the web version of this article).

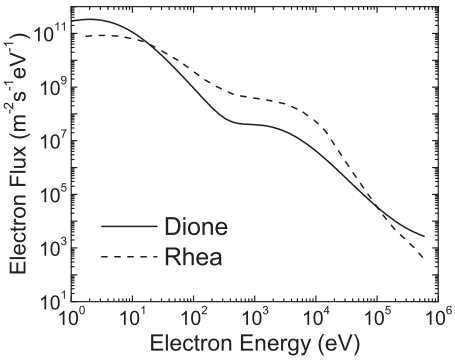

Fig. 17. The Dione and Rhea electron energy distribution functions from Schippers et al. (2008), used to estimate the Table 3 average electron–O_2 interaction rates.

the incident ions. By contrast channel 1 is simple charge exchange with O_2, and exhibits a large cross section at low H$^+$ speeds (long interaction times for charge transfer). Accordingly, as H$^+$ channel 1 already dominates the (Luna et al., 2005) data at 10 keV (Fig. 14), we assume here that it continues to dominate below 10 keV in the Williams et al. (1984) and Cabrera-Trujillo et al. (2004) data as well. H$^+$ channels 2–4 exhibit a constant log–log slope versus energy in the (Luna et al., 2005) data near 10 keV; we extrapolate these power law dependences to 'low energies' below 10 keV. Channel 4 exhibits a steep low energy slope with energy ($\sim E^1$) since this channel is the most energy intensive, involving (in addition to charge exchange) dissociation and electron ejection resulting in a doubly charged O ion. Channel 3 is similar but results in two O$^+$ ions, hence showing a shallower slope proportional to

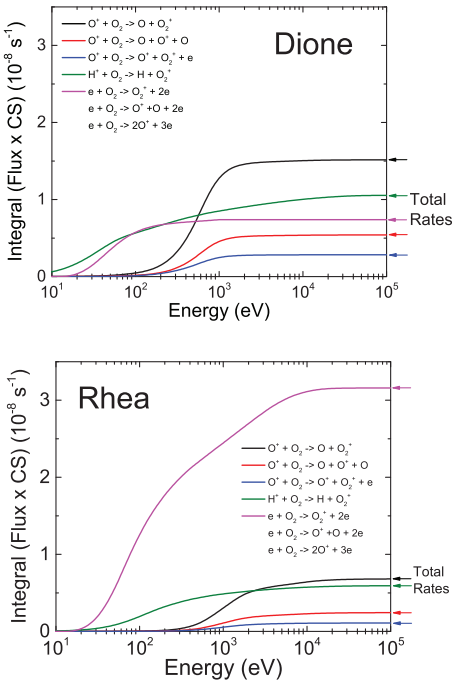

Fig. 18. The cumulative integration of Eq. (1) for Dione and Rhea, demonstrating the convolution of the interaction cross sections with the electron and ion energy distributions to estimate the Table 3 interaction rates. To simplify the plot we show only the most significant interaction channels and sum the electron channels.

ion speed ($\sim E^{1/2}$), as expected for formation of singly charged ions from adiabatic ion–neutral collisions (Linhard and Scharff, 1961). Channel 2 only involves charge exchange plus dissociation, without electron ejection, thereby exhibiting a shallow slope with energy ($\sim E^{1/4}$). Finally, to obtain channel 1 we subtracted the sum of 2–4 from the Williams et al. (1984) and Cabrera-Trujillo et al. (2004) total charge transfer data. The proportion of H^+ impact ionization in channels 5 and 6 is roughly constant with energy in the Luna et al. (2005) data. We continue the same apportionment between 5 and 6 below 10 keV, while assuming a proportionality of the ionization with projectile speed (or $E^{1/2}$). Channel 7 results in a doubly charged O ion and thereby exhibits a steep slope with energy ($\sim E^1$) in the (Luna et al., 2005) data, which we extrapolate below 10 keV.

As described earlier the Dione and Rhea exospheric time constants are (away from solstice) too long for transient magnetospheric variability to influence the exospheres. Accordingly, we estimated the velocity distribution functions of Saturn's electron and ion plasma from the CAPS and MIMI based Saturn system survey studies of Dialynas et al. (2009), Schippers et al. (2008), Thomsen et al. (2010), Wilson et al. (2008) and Wilson et al. (2010), which represent the best knowledge available on Saturn's average magnetospheric conditions. Using densities of 2.5(0.4) H^+ and 31(5) W^+ per cm^3 at Dione(Rhea), and parallel/perpendicular temperatures of 6/12(19/30) eV H^+ and 20/92(63/225) eV W^+ from Thomsen et al. (2010), Wilson et al. (2008) and Wilson et al. (2010), together with the high energy (>10 keV) suprathermal distribution functions of Dialynas et al. (2009), we reconstructed the velocity distribution functions $f_{H^+}(\vec{v})$ and $f_{W^+}(\vec{v})$ of the ion flux. These functions must be translated from the plasma co-rotation rest frame into the Dione and Rhea frames, i.e., $f_i(\vec{v}) \rightarrow f_i(\vec{v}')$, with $i = H^+$ or W^+, $\vec{v}' = \vec{v} + \vec{v}_0$ and $\vec{v}_0$ the co-rotation velocity relative to Dione (41 km/s) and Rhea (49 km/s). We also estimated (using an ion back tracing method as described by Teolis et al. (2010b) and Cassidy et al. (2013) the ion 'access' function $g(\vec{r}, \vec{v})$ of position and velocity, with values of 0 or 1 characterizing the cycloidal ion trajectories allowed ($g = 1$) or blocked ($g = 0$) by the body. We then integrated (numerically) the resulting position dependent velocity distribution $F_i(\vec{r}, \vec{v}) = g_i(\vec{r}, \vec{v}) f_i(\vec{v})$ over the exospheric volume V around the body, up to 100 km altitude, to estimate the globally averaged velocity distribution function $F_i^{\mathrm{avg}}(\vec{v}) = \int_V F_i(\vec{r}, \vec{v})\, d^3\vec{r}$. Finally, we integrated over 4π steradians of angular space to obtain the average distribution versus velocity magnitude v around the body, i.e., $F_i^{\mathrm{avg}}(v) = \int F_i^{\mathrm{avg}}(\vec{v}) d\Omega$, where $d\Omega = v^2 \cos\alpha\, d\alpha\, d\beta$ in terms of polar angle and azimuth α and β. In Fig. 15 we show the distributions versus velocity magnitude for H^+ and O^+ at Dione and Rhea. For electrons (at energies below 1 keV relevant for exospheric ionization) the gyroradii are much smaller than the body, and the guiding center drift is negligible, simplifying the analysis. Accordingly, for electrons we used the (Schippers et al., 2008) velocity distributions for the Dione and Rhea orbital radii, as shown in Fig. 16, without further processing.

The last step was to estimate the average interaction rates (Table 3) by convolving the cross sections ($\sigma(v)$ from Figs. 13–15) and distributions ($F^{\mathrm{avg}}(v)$ from Figs. 16 to 17), i.e.,

$$\mathrm{rate} = \int F^{\mathrm{avg}}(v)\, \sigma\,(v) dv. \quad (1)$$

In Fig. 18 we show the cumulative integrals (versus energy) to demonstrate the process.

References

Buratti, B.J., et al., 2011. Photometry of Triton 1992–2004: surface volatile transport and discovery of a remarkable opposition surge. Icarus 212, 835.

Burger, M.H., Killen, R.M., Vervack, R.J., et al., 2010. Monte Carlo modeling of sodium in Mercury's exosphere during the first two MESSENGER flybys. Icarus 209, 63.

Cabrera-Trujillo, R., Ohrn, Y., Deumens, E., et al., 2004. Absolute differential and total cross sections for direct and charge-transfer scattering of keV protons by O2. Phys. Rev. A 70, 042702.

Carlson, R.W., 1999. A tenuous carbon dioxide atmosphere on Jupiter's Moon Callisto. Science 283, 820.

Cassidy, T.A., 2008. Europa's Tenuous Atmosphere. University of Virginia, Charlottesville, Virginia.

Cassidy, T.A., Bagenal, F., Delamere, P.A., et al., 2012. Self-limiting sputtering at Europa. In: American Geophysical Union Fall Meeting 2012, edited.

Cassidy, T.A., Johnson, R.E., 2005. Monte Carlo model of sputtering and other ejection processes within a regolith. Icarus 176 (2), 499–507.

Cassidy, T.A., Johnson, R.E., Mcgrath, M.A., et al., 2007. The spatial morphology of Europa's near-surface O2 atmosphere. Icarus 191, 755.

Cassidy, T.A., Merkel, A.W., Burger, M.H., et al., 2015. Mercury's seasonal sodium exosphere: MESSENGER orbital observations. Icarus 248, 547.

Cassidy, T.A., Paranicas, C., Shirley, J.H., et al., 2013. Magnetospheric ion sputtering and water ice grain size at Europa. Planet. Space Sci 77, 64.

Christon, S.P., Hamilton, D.C., DiFabio, R.D., et al., 2013. Saturn suprathermal O2+ and mass-28+ molecular ions: Long-term seasonal and solar variation. J. Geophys. Res.: Space Phys. 118, 3446.

Ciarniello, M., et al., 2011. Hapke modeling of Rhea surface properties through Cassini-VIMS spectra. Icarus 214, 541.

Clark, R.N., et al., 2008. Compositional mapping of Saturn's satellite Dione with Cassini VIMS and implications of dark material in the Saturn system. Icarus 193, 372.

Crider, D.H., Vondrak, R.R., 2000. The solar wind as a possible source of lunar polar hydrogen deposits. J. Geophys. Res. 105, 26773.

Cruikshank, D.P., et al., 2010. Carbon dioxide on the satellites of Saturn: Results from the Cassini VIMS investigation and revisions to the VIMS wavelength scale. Icarus 206, 561.

Cruikshank, D.P., Owen, T.C., Ore, C.D., et al., 2005. A spectroscopic study of the surfaces of Saturn's large satellites: H2O ice, tholins, and minor constituents. Icarus 175, 268.

Cunningham, N.J., Spencer, J.R., Feldman, P.D., et al., 2015. Detection of Callisto's oxygen atmosphere with the Hubble Space telescope. Icarus 254, 178.

Dialynas, K., Krimigis, S.M., Mitchell, D.G., et al., 2009. Energetic ion spectral characteristics in the Saturnian magnetosphere using Cassini/MIMI measurements. J. Geophys. Res. 114, A01212.

Elrod, M.K., Tseng, W.-L., Woodson, A.K., et al., 2014. Seasonal and radial trends in Saturn's thermal plasma between the main rings and Enceladus. Icarus 242, 130.

Fulvio, D., Raut, U., Baragiola, R.A., 2012. Photosynthesis of carbon dioxide from carbon surfaces coated with oxygen: implications for interstellar molecular clouds and the outer solar system. Astrophys. J. Lett. 752, L33.

Giauque, W.F., Egan, C.J., 1937. Carbon dioxide. The heat capacity and vapor pressure of the solid. The heat of sublimation. Thermodynamic and spectroscopic values of the entropy. J. Chem. Phys. 5, 45.
Hall, D.T., Feldman, P.D., McGrath, M.A., et al., 1998. The far-ultraviolet oxygen airglow of Europa and Ganymede. Astrophys. J. 499 (1), 475–481.
Hou, W.-C., Chowdhury, I., Goodwin, D.G., et al., 2015. Photochemical transformation of graphene oxide in sunlight. Environ. Sci. Technol. 49, 3435.
Howett, C.J.A., et al., 2016. Thermal properties of Rhea's Poles: Evidence for a Meter-Deep Unconsolidated Subsurface Layer. Icarus doi:10.1016/j.icarus.2016.02.033.
Howett, C.J.A., Spencer, J.R., Hurford, T., et al., 2014. Thermophysical property variations across Dione and Rhea. Icarus 241, 239.
Howett, C.J.A., Spencer, J.R., Pearl, J., et al., 2010. Thermal inertia and bolometric Bond albedo values for Mimas, Enceladus, Tethys, Dione, Rhea and Iapetus as derived from Cassini/CIRS measurements. Icarus 206, 573.
Huebner, W.F., Keady, J.J., Lyon, S.P., 1992. Solar photo rates for planetary atmospheres and atmospheric pollutants. Astrophys. Space Sci. 195, 1.
Itikawa, Y., 2008. Cross sections for electron collisions with oxygen molecules. Inst. Space Astronaut. Sci. 38, 1.
Johnson, R.E., Carlson, R.W., Cassidy, T.A., et al., 2013. In: Gudipati, M.S., Castillo-Rogez, J. (Eds.), Sputtering of Ices, in *The Science of Solar System Ices*. Springer, New York.
Jones, G.H., et al. (2009), Rhea's interaction with Saturn's magnetosphere: Evidence for a plasma source, paper presented at American Geophysical Union, Fall Meeting 2009, San Francisco.
Killen, R.M., Hurley, D.M., Farrell, W.M., 2012. The effect on the lunar exosphere of a coronal mass ejection passage. J. Geophys. Res. 117, E00K02.
Killen, R.M., Sarantos, M., Potter, A.E., et al., 2004. Source rates and ion recycling rates for Na and K in Mercury's atmosphere. Icarus 171, 1.
Lifshitz, Y., Kasi, S.R., Rabalais, J.W., et al., 1990. Subplantation model for film growth from hyperthermal species. Phys. Rev. B 41, 10468.
Linhard, J., Scharff, M., 1961. Energy dissipation by ions in the kev region. Phys. Rev. 124, 128.
Luna, H., McGrath, C., Shah, M.B., et al., 2005. Dissociative charge exchange and ionization of O2 by fast H+ and O+ ions: Energetic ion interactions in Europa's oxygen atmosphere and neutral Torus. Astrophys. J. 628, 1086.
Marconi, M.L., 2007. A kinetic model of Ganymede's atmosphere. Icarus 190, 155.
Martens, H.R., Reisenfeld, D.B., Williams, J.D., et al., 2008. Observations of molecular oxygen ions in Saturn's inner magnetosphere. Geophys. Res. Lett. 35, L20103.
Matsumoto, Y., Koinuma, M., Ida, S., et al., 2011. Photoreaction of graphene oxide nanosheets in water. J. Phys. Chem. C 115, 19280.
McGrath, M.A., Jia, X., Retherford, K., et al., 2013. Aurora on Ganymede. J. Geophys. Res.: Space Phys. 118, 2043.
Noll, K.S., Roush, T.L., Cruikshank, D.P., et al., 1997. Detection of ozone on Saturn's satellites Rhea and Dione. Nature 388 (6637), 45–47.
Paige, D.A., Siegler, M.A., Harmon, J.K., et al., 2012. Thermal stability of frozen volatiles in the North Polar region of Mercury. In: LPSC, edited. Woodlands, Texas, p. 2875.
Paige, D.A., et al., 2010. Diviner lunar radiometer observations of cold traps in the Moon's South Polar region. Science 330, 479.
Petrik, N.G., Monckton, R.J., Koehler, S.P.K., et al., 2014. Distance-dependent radiation chemistry: Oxidation versus hydrogenation of CO in electron-irradiated H2O/CO/H2O ices. J. Phys. Chem. C 118, 27483.
Plainaki, C., Milillo, A., Massetti, S., et al., 2015. The H2O and O2 exospheres of Ganymede: The result of a complex interaction between the jovian magnetospheric ions and the icy moon. Icarus 245, 306.
Plainaki, C., Milillo, A., Mura, A., et al., 2010. Neutral particle release from Europa's surface. Icarus 210, 385.
Plainaki, C., Milillo, A., Mura, A., et al., 2012. The role of sputtering and radiolysis in the generation of Europa exosphere. Icarus 218, 956.
Poppe, A.R., Halekas, J.S., Sarantos, M., et al., 2013. The self-sputtered contribution to the lunar exosphere. J. Geophys. Res.: Planets 118, 1934.
Raut, U., Baragiola, R.A., 2013. Sputtering and molecular synthesis induced by 100 keV protons in condensed CO2 and Relevance to the outer Solar System. Astrophys. J. 772, 53.
Raut, U., Fulvio, D., Loeffler, M.J., et al., 2012. Radiation synthesis of carbon dioxide in ice-coated carbon: Implications for interstellar grains and icy moons. Astrophys. J. 752, 159.
Rook, F.L., Johnson, R.E., Brown, W.L., 1985. Electronic sputtering of solid N2 and O2: A comparison on non-radiative processes. Surface Sci. 164, 625.
Roussos, E., Muller, J., Simon, S., et al., 2008. Plasma and fields in the wake of Rhea: 3-D hybrid simulation and comparison with Cassini data. Annales Geophys. 26, 619.
Sabri, T., et al., 2015. A laboratory study of ion-induced erosion of ice-covered carbon grains. Astron. Astrophys. 575, A76.
Saur, J., Feldman, P.D., Roth, L., et al., 2011. Hubble space telescope/advanced camera for surveys observations of Europa's atmospheric ultraviolet emission at eastern elongation. Astrophys. J. 738, 153.
Saur, J., Strobel, D.F., 2005. Atmospheres and plasma interactions at saturn's largest inner icy satellites. Astrophys. J. 620, L115.
Schippers, P., et al., 2008. Multi-instrument analysis of electron populations in Saturn's magnetosphere. J. Geophys. Res. 113, A07208.
Schorghofer, N., Taylor, G.J., 2007. Subsurface migration of H2O at lunar cold traps. J. Geophys. Res. 112, E02010.
Scipioni, F., Tosi, F., Stephan, K., et al., 2014. Spectroscopic classification of icy satellites of Saturn II: Identification of terrain units on Rhea. Icarus 234, 1.
Scipioni, F., Tosi, F., Stephan, K., et al., 2013. Spectroscopic classification of icy satellites of Saturn I: Identification of terrain units on Dione. Icarus 226, 1331.
Shematovich, V.I., Johnson, R.E., Cooper, J.F., et al., 2005. Surface-bounded atmosphere of Europa. Icarus 173, 480.
Shi, J., Grieves, G.A., Orlando, T.M., 2015. Vacuum ultraviolet photon-stimulated oxidation of buried ice: Graphite grain interfaces. Astrophys. J. 804, 24.
Shim, J.-Y., 2001. The Temporal Evolution of the Lunar Exosphere. University of Texas at Austin, Austin, Texas.
Sieglaff, D.R., Lindsay, B.G., Merrill, R.L., et al., 2000. Absolute differential and integral cross sections for charge transfer of keV O+ ions with O2. J. Geophys. Res. 105, 10631.
Siegler, M.A., Bills, B.G., Paige, D.A., 2012. Spatio-temporal evolution of lunar cold traps. In: LPSC, edited. Woodlands, Texas, p. 2376.
Simon, S., Saur, J., Neubauer, F.M., et al., 2011. Magnetic signatures of a tenuous atmosphere at Dione. J. Geophys. Res. 38, L15102.
Sittler, E.C., Johnson, R.E., Jurac, S., et al., 2004. Pickup ions at Dione and Enceladus: Cassini Plasma spectrometer simulations. J. Geophys. Res. 109, A01214.
Smyth, W.H., Marconi, M.L., 2006. Europa's atmosphere, gas tori, and magnetospheric implications. Icarus 181, 510.
Srama, R., et al., 2011. The cosmic dust analyser onboard cassini: ten years of discoveries. CEAS Space J. 2, 3.
Stephan, K., et al., 2012. The Saturnian satellite Rhea as seen by Cassini VIMS. Planetary Space Sci. 61, 142.
Stephan, K., et al., 2010. Dione's spectral and geological properties. Icarus 206, 631.
Tang, K.B.K., Azria, R., Coat, Y.L., et al., 1996. O- ESD from O2 monolayers physisorbed on graphite: a surface mediated mechanism. Zeitschrift fur Physik D 38, 41.
Teolis, B.D., et al., 2010a. Cassini finds an oxygen–carbon dioxide atmosphere at Saturn's icy moon Rhea. Science 330, 1813.
Teolis, B.D., et al., 2010b. Cassini finds an oxygen–carbon dioxide atmosphere at Saturn's icy moon Rhea. Science (Supporting Online Material) 330, 1813.
Teolis, B.D., Loeffler, M.J., Raut, U., et al., 2006. Ozone synthesis on the icy satellites. Astrophys. J. 644, L141.
Teolis, B.D., et al., 2015. A revised sensitivity model for Cassini INMS: results at Titan. Space Sci. Rev. 186 (388), 1.
Teolis, B.D., Shi, J., Baragiola, R.A., 2009. Formation, trapping, and ejection of radiolytic O_2 from ion-irradiated water ice studied by sputter depth profiling. J. Chem. Phys. 130, 134704.
Teolis, B.D., Sillanpää, I., Waite, J.H., et al., 2014. Surface current balance and thermoelectric whistler wings at airless astrophysical bodies: Cassini at Rhea. J. Geophys. Res. Space Phys. 119, 8881.
Teolis, B.D., Vidal, R.A., Shi, J., et al., 2005. Mechanisms of O_2 sputtering from water ice by keV ions. Phys. Rev. B 72, 245422.
Teolis, B.D., Waite, J.H., 2012. Cassini measurements show seasonal O2 – CO2 exospheres and possible seasonal CO2 frosts at Rhea and Dione. In: LPSC, edited. Woodlands, Tx, USA.
Thomsen, M.F., Reisenfeld, D.B., Delapp, D., et al., 2010. Survey of ion plasma parameters in Saturn's magnetosphere. J. Geophys. Res. 115, A10220.
Tokar, R.L., Johnson, R.E., Thomsen, M.F., et al., 2012. Detection of exospheric O2+ at Saturn's moon dione. J. Geophys. Res. 39, L03105.
Tseng, W.-L., Johnson, R.E., Elrod, M.K., 2013. Modeling the seasonal variability of the plasma environment in Saturn's magnetosphere between main rings and Mimas. Planet. Space Sci. 77, 126.
Vorburger, A., Wurz, P., Lammer, H., et al., 2015. Monte-Carlo simulation of Callisto's exosphere. Icarus 262, 14.
Waite, J.H., et al., 2004. The Cassini ion and neutral mass spectrometer (INMS) investigation. Space Sci. Rev. 114, 113.
Williams, I.D., Geddes, J., Gilbody, H.B., 1984. Electron capture, loss and axcitation in collisions of H+, H(1 s), H(2 s) and H- in atomic oxygen. J. Phys. B: Atomic Mol. Phys. 17, 1547.
Wilson, R.J., F. Crary, L.K. Gilbert, et al. (2012), PDS user's guide for Cassini plasma spectrometer (CAPS)*Rep.*, Planetary Data System, Available at http://ppi.pds.nasa.gov/.
Wilson, R.J., Tokar, R.L., Henderson, M.G., et al., 2008. Cassini plasma spectrometer thermal ion measurements in Saturn's inner magnetosphere. J. Geophys. Res. 113, A12218.
Wilson, R.J., Tokar, R.L., Kurth, W.S., et al., 2010. Properties of the thermal ion plasma near Rhea as measured by the Cassini plasma spectrometer. J. Geophys. Res. 115, A05201.
Yakshinskiy, B.V., Madey, T.E., Ageev, V.N., 2000. Thermal desorption of sodium atoms from thin SiO2 films. Surface Rev. Lett. 7, 75.
Young, D.T., et al., 2004. Cassini plasma spectrometer investigation. Space Sci. Rev. 114, 1.
Young, L.A., 2013. Pluto's seasons: new predictions for new horizons. Astrophys. J. Lett. 766, L22.
Yuan, C., Cooke, I.R., Yates, J.T., 2014. A new source of CO2 in the universe: A photoactiviated Edel-Rideal surface reactions on water ices. Astrophys. J. Lett. 791, L21.